Thermal Modulation of Gigahertz Surface Acoustic Waves on Lithium Niobate

Linbo Shao,[1,2,*] Sophie W. Ding,[1] Yunwei Ma,[2,3] Yuhao Zhang,[2,3] Neil Sinclair,[1,4] and Marko Lončar[1,†]

[1] *John A. Paulson School of Engineering and Applied Sciences, Harvard University, Cambridge, Massachusetts 02138, USA*
[2] *Bradley Department of Electrical and Computer Engineering, Virginia Tech, Blacksburg, Virginia 24061, USA*
[3] *Center for Power Electronics Systems (CPES), Virginia Tech, Blacksburg, Virginia 24061, USA*
[4] *Division of Physics, Mathematics and Astronomy, and Alliance for Quantum Technologies (AQT), California Institute of Technology, Pasadena, California 91125, USA*

(Received 29 March 2022; revised 12 October 2022; accepted 27 October 2022; published 23 November 2022)

Surface-acoustic-wave (SAW) devices have a wide range of applications in microwave signal processing. Microwave SAW components benefit from higher quality factors and much smaller crosstalk when compared to their electromagnetic counterparts. Efficient routing and modulation of SAWs are essential for building large-scale and versatile acoustic wave circuits. Here, we demonstrate integrated thermoacoustic modulators using two SAW platforms: bulk lithium niobate and thin-film lithium niobate on sapphire. In both approaches, the gigahertz-frequency SAWs are routed by integrated acoustic waveguides, while on-chip microheaters are used to locally change the temperature, and thus, control the phase of the SAW. Using this approach, we achieve phase changes of over 720° with the responsibility of 2.6°/mW for bulk lithium niobate and 0.52°/mW for lithium niobate on sapphire. Furthermore, we demonstrate amplitude modulation of SAWs using acoustic Mach-Zehnder interferometers. Our thermoacoustic modulators can enable reconfigurable acoustic signal processing for next-generation wireless communications and microwave systems.

DOI: 10.1103/PhysRevApplied.18.054078

I. INTRODUCTION

Surface-acoustic-wave (SAW) devices [1–4] are widely used in microwave signal processing to realize oscillators, microwave filters, and delay lines. This is because the SAW propagates at a velocity that is 5 orders of magnitude smaller than that of an electromagnetic wave at the same frequency, and thus, SAW devices have much smaller wavelengths than their electromagnetic counterparts. This enables high-density integration and reduced crosstalk between SAW devices, which is leveraged to achieve efficient compression, correlation, and Fourier transform of radio-frequency (rf) pulses, for example, in a compact footprint. Acoustic wave devices have successfully pushed their operating frequency to tens of gigahertz [5–9], and thus, have become a promising platform for microwave signal processing for next-generation wireless communications.

The SAW also serves as a versatile interface between different quantum bits (qubits), including electron spins [10–12], superconducting qubits [13–20], and optical photons [20–25]. SAW devices utilize piezoelectric materials, such as ST-X quartz [14], aluminum nitride (AlN) [13,20,26–29], scandium-doped aluminum nitride (ScAlN) [30–32], gallium arsenide (GaAs) [18,19], gallium nitride (GaN) [33], zinc oxide (ZnO) [34], lithium tantalate [35,36], and lithium niobate (LN) [15–17,21,22,37–42], to convert signals between electromagnetic waves and acoustic waves. To date, most acoustic devices are linear, passive, and reciprocal components, which limit their functionality. Several efforts have been made to develop nonlinear, active, and nonreciprocal SAW devices. For example, nonreciprocal acoustic devices are demonstrated by circulating fluids [43], spatiotemporal modulations [44,45], acoustoelectric coupling in semiconductors [46,47], magnetoelastic coupling [48], and non-Hermitian physics [49–51]. Tunable SAW devices are achieved using mechanical nonlinear deformations [52], piezoelectrically actuated deformation [53], and electroacoustic effects [45] but still require high voltages to achieve a full π-phase shift.

Here, we demonstrate stable and efficient modulation of acoustic waves propagating on both bulk and thin-film LN-on-sapphire (LNSa) [40] substrates. Our approach leverages the temperature dependence of LN elasticity [54]

*shaolb@vt.edu
†loncar@seas.harvard.edu

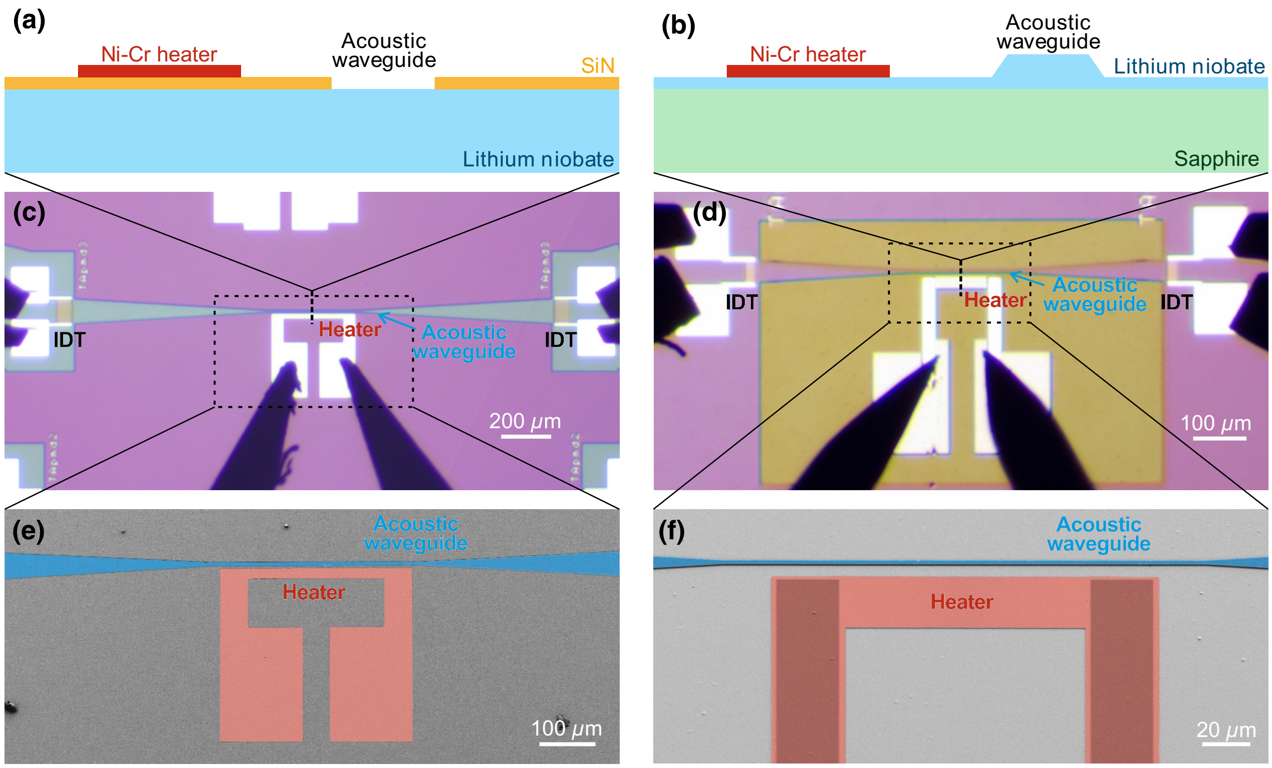

FIG. 1. Integrated thermoacoustic modulators based on bulk LN in (a),(c),(e) and thin-film LNSa in (b),(d),(f). (a),(b) Illustrations of the cross sections of the thermoacoustic modulators. Nanofabricated microheaters made of Ni-Cr alloy are used to tune the temperature of the acoustic waveguides defined by (a) an opening (slot) made of silicon nitride (SiN) film or (b) by etching the LN film (c),(d) Optical microscopy images of thermoacoustic modulators. Interdigital transducers (IDTs) are used to excite and detect acoustic waves. Microwave ground-signal (*GS*) probes are used to contact the IDT electrodes, and low-frequency probes are used to deliver current to the microheaters. Dashed boxes indicate the magnified regions shown in (e),(f). (e),(f) False-colored scanning-electron-microscopy (SEM) images of thermoacoustic modulators.

to control the phase velocity of acoustic waves by tuning the temperature of the waveguide that the waves propagate in. This is accomplished using microheaters located close to the acoustic waveguides (Fig. 1). Our thermoacoustic modulators provide an efficient and stable approach to control SAWs on chips, paving the way for more versatile acoustic wave microwave-signal-processing circuits.

II. DESIGN AND FABRICATION OF THERMOACOUSTIC MODULATORS

Our thermoacoustic modulators include acoustic waveguides, microheaters, and interdigital transducers (IDTs). Acoustic waves are generated piezoelectrically by the IDT, tapered into the acoustic waveguide, and tapered out to another IDT region where they are detected [Figs. 1(c) and 1(d)]. The microheater is situated adjacent to the waveguide.

For the bulk LN platform, we use a 128° *Y*-cut black LN substrate (the acoustic waves propagate in the crystal's *X* direction), which allows efficient IDTs on the bulk substrate. The electromechanical coupling efficiency, k^2, for the IDT is about 5.5%. In this demonstration, the acoustic wavelength is set to 2.8 μm at the IDT region for the bulk LN platform. The acoustic waveguides are defined by opening a slot in the overlay SiN thin film [45] [Fig. 1(a)]. Since SiN is a harder (larger stiffness coefficients) material, it allows a larger acoustic velocity than that of LN. Thus, a 7-μm-wide slot in the SiN thin film will create a region with lower acoustic velocity and guide the acoustic waves. The SiN thin film is deposited by plasma-enhanced chemical vapor deposition and patterned by photolithography using a laser direct writer and reactive-ion etching (RIE) using carbon tetrafluoride (CF_4) and trifluoromethane (CHF_3) gases. The thickness of SiN is about 500 nm, which allows efficient guiding of gigahertz acoustic waves and feasibility in fabrication.

For the LNSa platform, we use 620-nm-thick *X*-cut LN on a sapphire substrate, and the acoustic wave propagates in the *Y* direction of the LN crystal. The acoustic wavelength is chosen to be 1.7 μm at the IDT region, which yields an optimal electromechanical coupling efficiency, k^2, as high as 20% for the shear mode [40]. The pitch of the IDT is half of the acoustic wavelength. The acoustic

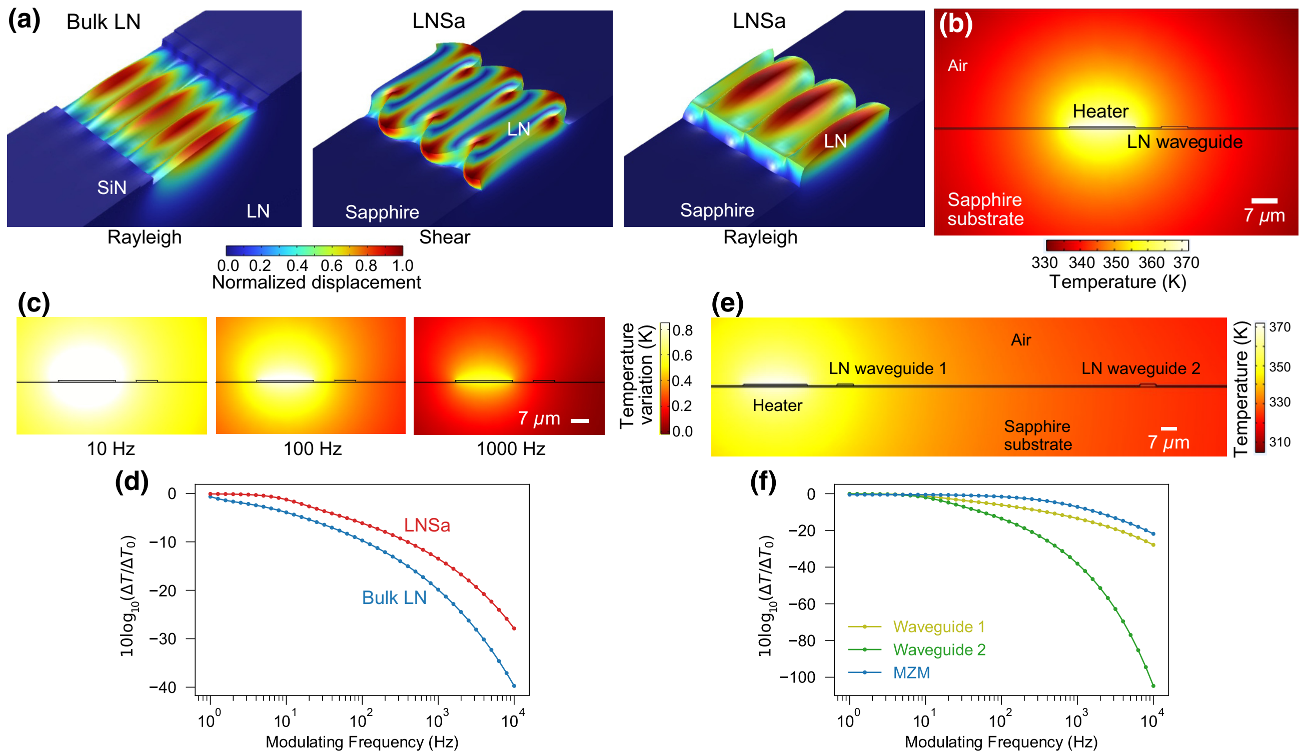

FIG. 2. Simulation of thermoacoustic modulators. (a) Acoustic waveguide simulation of the acoustic modes in the bulk LN and LNSa modulator. (b) Steady-state thermal response of the LNSa modulator: relative location and size of the waveguide and electrode are consistent with the fabricated device. Heat map indicates temperature. (c) Perturbative solutions at specific modulation frequencies for the LNSa modulator: as the frequency increases, the thermal response, and therefore, the phase modulation of the waveguide, is suppressed. (d) Frequency response of thermally driven bulk LN and LNSa phase modulators. (e) Cross-section geometry of the Mach-Zehnder modulator (MZM) and the heat map of the steady-state solution. (f) Frequency response of thermally driven LNSa MZM. Phase modulation of each arm is also shown.

rib waveguide is 7 μm in top width and etched down by 550 nm by RIE using argon gas [Fig. 1(b)]. The sidewall angle is about 70°. The acoustic waveguide supports the fundamental Rayleigh and shear modes [Fig. 2(a)]. The propagation losses of the acoustic waveguides were previously investigated for both the bulk LN [45] and LNSa platforms [40].

On both platforms, aluminum (Al) IDTs are patterned by a lift-off process with a thickness of 120 nm (100 nm) for the bulk LN (LNSa) devices. Al is deposited by electron-beam evaporation or thermal evaporation, and we find no performance differences between the two deposition processes. The microheaters are defined by another layer of lift-off process with nickel-chromium (Ni-Cr, 80/20 wt %, electrical resistivity $\rho = 1.9 \times 10^{-6}$ Ω m) using electron-beam evaporation. We design microheaters with dimensions of 10 to 25 μm in width, 100 to 250 μm in length, and 100 to 200 nm in thickness, which result in electric resistances from 40 to 500 Ω for different devices and applications. To reduce the contact resistance between the microheater and its contact pads, an additional 100-nm-thick Al layer is deposited on the Ni-Cr layer, as shown by the darker area in Fig. 1(f). The microheaters are placed with a minimum edge-to-edge clearance of 6 μm to ensure that the microheater does not cause additional propagation loss to the acoustic waves.

III. SIMULATION OF THERMOACOUSTIC MODULATION

We conduct numerical simulations to investigate the performance of the thermoacoustic modulators. We simulate the waveguide modes and the thermal response of the devices using finite-element-method simulations in COMSOL Multiphysics (Fig. 2). For the simulation of the guided acoustic modes, Bloch boundary conditions are imposed for the waveguide, so that the eigenmodes correspond to the guided modes with the same wavelength. The modes with distinct displacements at the lowest frequencies are the fundamental modes. There are two types of modes in the LNSa waveguide, the shearing and Rayleigh modes [Fig. 2(a)], at 2.7 and 2.9 GHz, respectively, with an acoustic wavelength of 1.4 μm in the waveguide. Notably, in the IDT region, the acoustic wavelength is 1.7 μm at the same frequency, which is longer than that in the waveguide; this is due to the larger acoustic velocity at the IDT region than

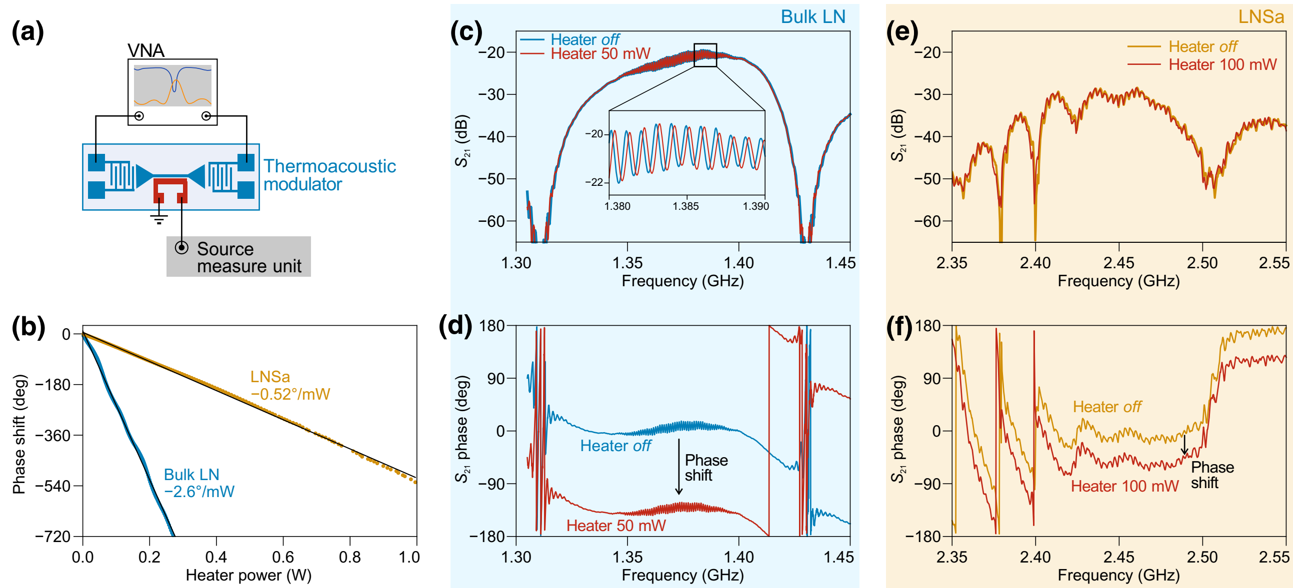

FIG. 3. Experimental characterization of the thermoacoustic phase modulators on bulk LN and LNSa. (a) Experimental setup. VNA measures the S parameters of the modulator, and a source measure unit applies voltage to the microheater while measuring the current. (b) Phase shift for various powers applied to the heater. Phase shift is measured at SAW frequencies of 1.385 and 2.46 GHz in the case of the bulk LN and LNSa modulator, respectively. We speculate that the periodic variations seen in the case of the bulk LN device are caused by the instability of the source used to control the heater power. Transmission measurement with heaters *off* and *on* for (c),(d) bulk LN modulator and (e),(f) LNSa modulator. (c),(e) Amplitudes of S_{21} are not affected by the heater. (d),(f) Phases of S_{21} are shifted by the heater. Linear frequency-phase responses of S_{21} due to the acoustic wave group delays are subtracted in (d),(f).

that at the waveguide. For the bulk LN waveguides, the relevant mode is a Rayleigh mode at 1.4 GHz with an acoustic wavelength of 2.9 μm [Fig. 2(a)].

The thermal response of the modulator is simulated at a cross section of the device perpendicular to the SAW propagation direction [Fig. 2(b)]. The device is simulated in quasi-three dimensions at room temperature (293.15 K) and atmosphere, with periodic boundary conditions applied to the surfaces of the cross-section slice. The fixed-temperature boundary condition is applied to the other surfaces of the domain. We perform simulations with different domain sizes to ensure the validity of our results. The heater electrode is modeled as the heat source, and heat propagates through the materials and brings the waveguide to a higher temperature in the steady-state solution [Fig. 2(b)].

To study the frequency-domain behavior of the bulk LN and LNSa modulator, we modulate the power applied to the electrode, which can be treated as a perturbation to the steady-state solution. We simulate the waveguide temperature variation as a function of the modulation frequency. The 3-dB cutoff frequency for thermal modulation is 8 Hz (20 Hz) for the bulk LN (LNSa) modulator [Fig. 2(d)]. The difference in the frequency response of the two modulators reflects the difference in the material's thermal conductivity, as sapphire is more thermally conductive than bulk LN.

To achieve amplitude modulation of acoustic waves, we demonstrate a LNSa thermoacoustic Mach-Zehnder modulator (MZM). The MZM utilizes the phase difference between two arms (waveguides) to achieve amplitude modulation via interference when two arms are merged at the output. To construct thermoacoustic MZMs, we place the microheater at different distances away from the two acoustic waveguides, and thus, the SAW in each arm accumulates different phases. Intuitively, the output of the MZM depends on the temperature difference between two waveguides. This is different from the phase modulator, in which the temperature of individual waveguides compared to the environmental temperature determines the phase shift. Therefore, the MZM shows a 3-dB-modulation bandwidth of about 400 Hz, which is much higher than that of the phase modulator [Fig. 2(f)]. The microheater is placed 6 μm away from the waveguide in one arm, but 106 μm away from the waveguide in the other.

IV. EXPERIMENTAL CHARACTERIZATION OF THERMOACOUSTIC PHASE MODULATORS

We experimentally measure the S parameters of the thermoacoustic phase modulators using a vector network analyzer (VNA), while controlling the power applied to the microheater [Fig 3(a)]. The IDTs are connected by microwave *GS* probes (GGB 40A), and the microheaters

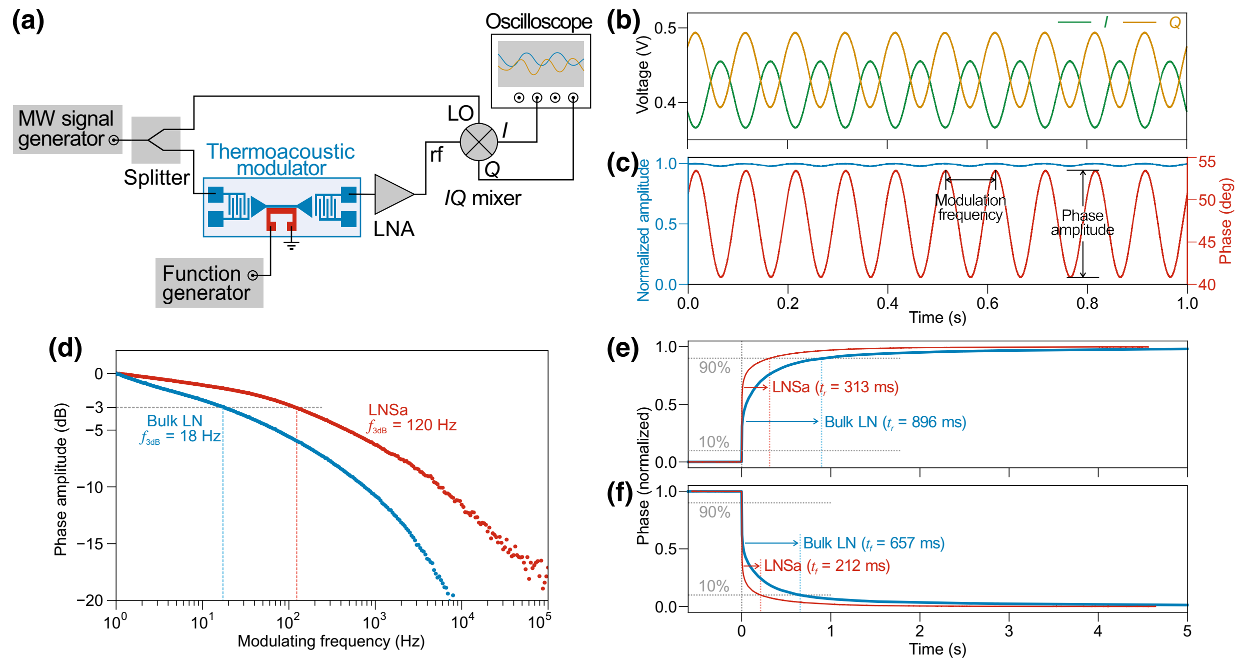

FIG. 4. Characterization of the frequency and transient response of thermoacoustic phase modulators. (a) Experimental setup. Microwave (MW) signal generator provides a source signal at 1.385 GHz for the bulk LN modulator and 2.44 GHz for the LNSa modulator. Source signal is split into two paths: one connects the input IDT of the device, and the other one feeds the local-oscillator (LO) input of an *IQ* mixer. Function generator applies a time-varying signal to the microheater. Modulated signal from the output IDT is amplified by a low-noise amplifier (LNA) and downconverted by the *IQ* mixer. *IQ* signals are finally measured with an oscilloscope. (b) Measured *I* and *Q* signals and (c) calculated amplitude and phase of the LNSa modulator output when a 10-Hz sine wave with amplitude of 0.3 V and offset of 3.5 V is applied to the heater. (d) Frequency response of the phase amplitude for the bulk LN and the LNSa modulator. Transient response of the output phase when the heater is (e) turned *on* and (f) turned *off* by a square wave. Step voltage is set to 3 V for the bulk LN modulator and 3.5 V for the LNSa modulator to achieve phase shifts of about 120°.

are contacted by low-frequency probes. The amplitude and phase of S parameters are calibrated to the probes. We control the phase of the output acoustic waves by tuning the power delivered to the microheaters [Fig. 3(b)]. The bulk LN modulator exhibits a phase response of −2.6°/mW, compared to only −0.52°/mW for the LNSa modulator. The phase shift is measured at the optimal frequencies with largest transmission S_{21}. The response of the phase shift to the applied microheater power is linear.

We measure the transmission S_{21} spectra of our modulators when the microheater is switched *on* and *off* [Figs. 3(c)–3(f)]. The acoustic wave bandwidths of our thermoacoustic modulators are determined by their IDTs. The acoustic wave bandwidth is about 90 MHz (from 1.33 to 1.42 GHz) for the bulk LN modulator [Fig. 3(c)] and about 70 MHz (from 2.41 to 2.48 GHz) for the LNSa modulator [Fig. 3(e)]. As expected for phase modulators, the amplitude of S_{21} does not change when the heater is switched *on* [Figs. 3(c) and 3(e)], while the phase of S_{21} is shifted [Figs. 3(d) and 3(f)]. The S_{21} phases in Figs. 3(d) and 3(f) are offset by the delay time at the central frequencies of each device. For the LNSa modulator, we note that different types of acoustic waves might be excited by the IDT simultaneously, and thus, lead to different dispersions (delay times) and interference in the 2.35–2.40-GHz frequency range. Overall, our thermoacoustic modulator can provide a phase shift over frequencies within their IDT bandwidths.

V. FREQUENCY RESPONSE OF THERMOACOUSTIC MODULATORS

We now characterize the frequency response of our thermoacoustic modulators. A function generator provides small signals at different frequencies and dc offsets to the microheater [Fig. 4(a)]. A microwave signal generator provides continuous signals at frequencies with maximum transmission: 1.385 GHz for the bulk LN modulator and 2.44 GHz for the LNSa modulator. A commercial in-phase quadrature (*IQ*) mixer is used to downconvert the output SAW signals to low-frequency in-phase (*I*) and quadrature (*Q*) signals [Fig. 4(b)], which are captured by an oscilloscope and converted into the amplitude and phase of the output acoustic waves [Fig. 4(c)]. Ideally, the phase modulators do not change the amplitude of the SAW. The observed small variation in the amplitude of the output acoustic waves might be due to the interference between

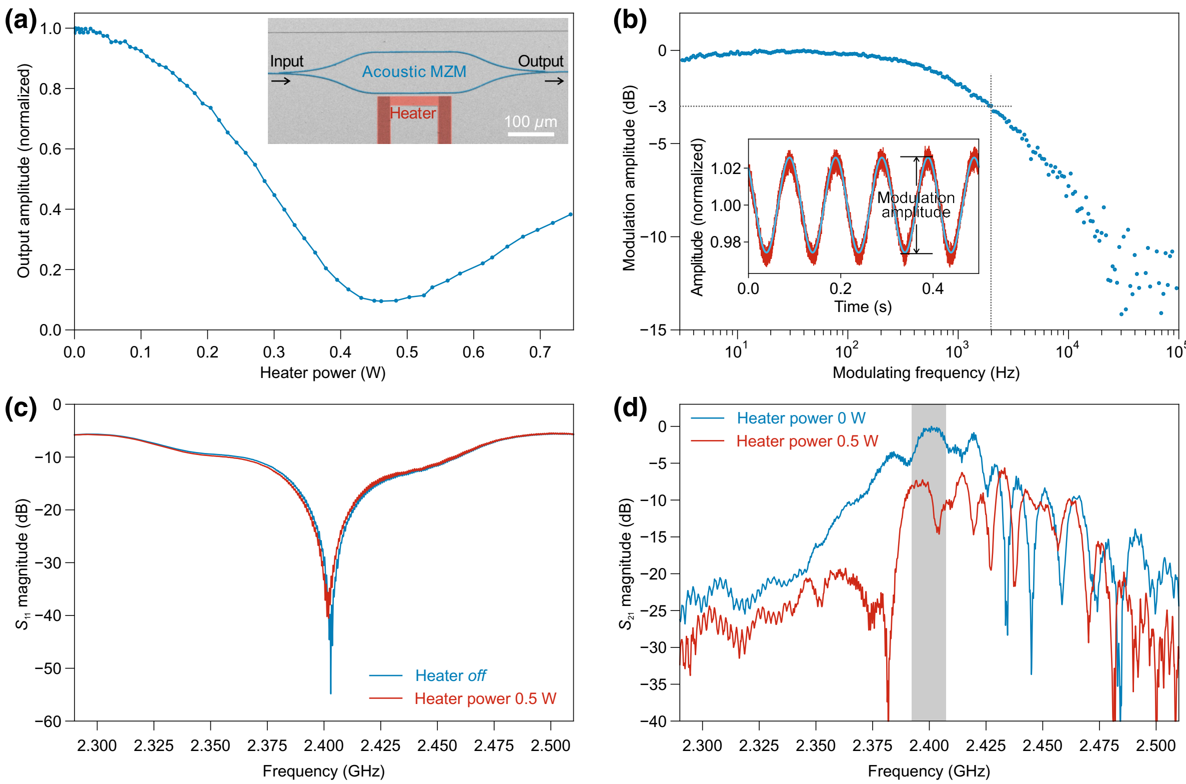

FIG. 5. Characterization of a thermoacoustic MZM. (a) Amplitude of the output acoustic wave for varied heater power. Inset, SEM image of a thermoacoustic MZM. (b) Frequency response of the MZM. Inset, modulated amplitude of the output acoustic waves. (a),(b) Same setup as that shown in Fig. 4(a) is used to characterize the device, and the amplitude is calculated from the I and Q signals captured by the oscilloscope. (c) S_{11}- and (d) S_{21}-parameter measurements of the thermoacoustic MZM with the heater *off* and at 0.5 W. Same setup as that shown in Fig. 3(a) is used to measure the S parameters in (c),(d). Thermoacoustic MZMs are fabricated on the LNSa platform. Devices used in (a),(b) and (c),(d) are of the same design but from different fabrication batches, and thus, the central frequencies are slightly different. Central frequency for the device in (a),(b) is 2.45 GHz and that in (c),(d) is 2.40 GHz.

different types of acoustic waves or misalignment of I and Q signals.

The measured frequency responses show a 3-dB bandwidth of 18 Hz for the bulk LN modulator and a higher bandwidth of 120 Hz for the LNSa modulator [Fig. 4(d)]. We speculate that the differences between the measured results and numerical simulations are due to the following factors: (1) our simulation is quasi-three dimensional and does not take the length of the heater into account, while the fabricated microheater has a limited length; (2) the material properties that are used in simulations may not be accurate for black LN and LN thin films.

We also characterize the transient response for large signals applied to the microheaters. We apply a step function with a low voltage of 0 V and a high voltage of 3 V (3.5 V) for the bulk LN (LNSa) modulator. We observe a rise time of 896 ms (313 ms) when turning *on* the microwave heater for the bulk LN (LNSa) modulator and a fall time of 657 ms (212 ms) when switching it *off*. The transient response times for large signals are longer than the transient times converted from their 3-dB bandwidths. The difference between the rise and fall times reflects the different time constants in the heating and cooling procedures, which are not symmetric. For heating, the acoustic waveguide is heated by the nearby microheater, while for cooling the heat is dissipated to the environment. We also note that the transient curves shown in Figs. 4(e) and 4(f) are not exponential due to the complex thermal response of our thin-film stacks.

VI. THERMOACOUSTIC MACH-ZEHNDER MODULATOR

We use the LNSa platform to demonstrate the thermoacoustic MZM [Fig. 5(a), inset]. Using the same setup as that shown in Fig. 4(a), we measure the output acoustic amplitude at various heater powers [Fig. 5(a)]. For an input acoustic frequency of 2.45 GHz, the minimum output amplitude is observed at a heater power of 0.45 W, and the minimum output power is about 10% of the maximum output power when the heater is *off*, resulting in an extinction ratio of about 10 dB. We further measure the frequency response of the thermoacoustic MZM. The heater is biased

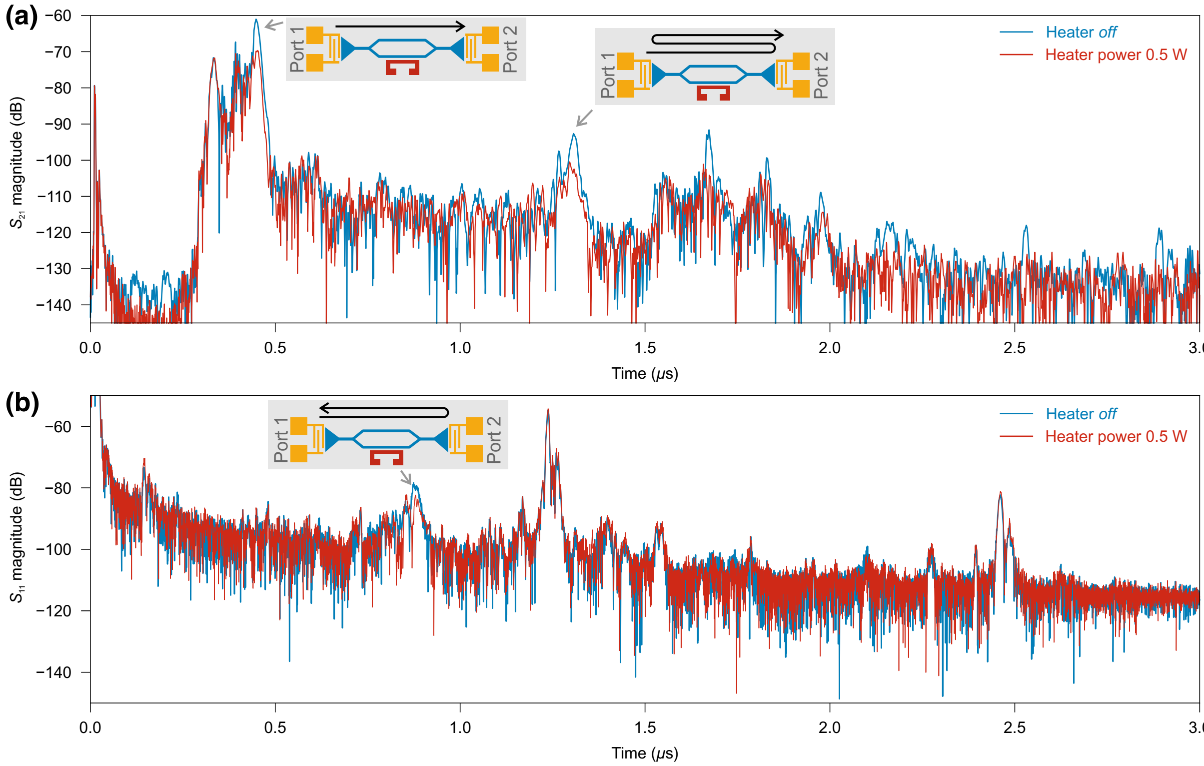

FIG. 6. Time-domain analysis of the thermoacoustic MZM. Multiple peaks observed in (a) transmission and (b) reflection signals indicate possible involvement of multiple acoustic modes and reflections. Single-pass traveling time for the main acoustic mode is about 450 ns. Central frequency for time-domain analysis is 2.40 GHz. Corresponding S parameters are shown in Figs. 5(c) and 5(d).

at about 0.2 W, and small signals with various frequencies are applied to the heater. The modulation amplitude is obtained from the captured I and Q signals [Fig. 5(b)]. Here, we observe the 3-dB bandwidth of 2.0 kHz for the thermoacoustic MZI modulator, which is much larger than that of the phase modulator, as expected. Generally, a shorter lateral distance between two MZM arms will result in a larger modulation bandwidth. However, reducing the lateral distance between two arms will reduce the temperature difference, and thus, reduce the modulation amplitude at low frequency.

The limited extinction ratio (∼10 dB) of amplitude modulation may be due to (1) uneven power splitting between two MZM arms or (2) coupling to higher-order acoustic modes, which have different propagation constants. Comparing the S-parameter spectra with the heater *off* and *on* [Figs. 5(c) and 5(d)], we observe that the extinction ratio is frequency dependent. The interference patterns between 2.42 and 2.45 GHz in Fig. 5(d) indicate possible involvement of multiple acoustic modes in our MZM. The S_{11} spectra are mainly defined by the IDTs, and we observe good impedance matching at the central frequency. Furthermore, we perform time-domain measurements and analysis (Keysight P5004A) of the acoustic MZM (Fig. 6). The multiple peaks in the transmission (S_{21}) and reflection (S_{11}) signals also infer the existence of multiple modes and reflections. The single-pass travel time of the acoustic wave is about 450 ns. In addition, we optically image the profiles of guided acoustic waves and observe patterns supporting mixing with higher-order modes (data not shown). Future developments and optimizations are needed to improve the extinction ratio of acoustic MZMs for practical applications.

VII. STABILITY OF THE THERMOACOUSTIC PHASE MODULATOR

Stability over time is one of the critical specifications for SAW devices. To characterize the stability, we measure the output of our thermoacoustic phase modulator over different time frames of 100 s and 1 h (Fig. 7). The heater is driven at a power of 0.2 W. We observe a variation in phase within a 0.15° (0.5°) range over 100 s (1 h) (Fig. 7). We speculate that the remaining phase variations are due to temperature fluctuations in the environment. We note that thermally controlled LN modulators feature better stability over a longer time than our previous modulators based on electrical fields [45].

VIII. DISCUSSION AND OUTLOOK

We demonstrate the thermal modulation of GHz acoustic waves propagating in two platforms: bulk LN and

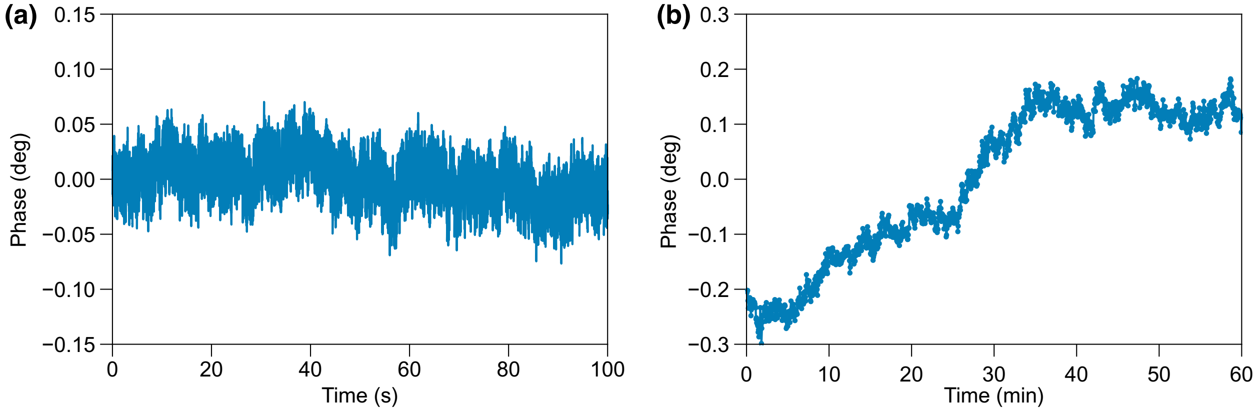

FIG. 7. Characterization of the stability of thermoacoustic phase modulators. Phase of the acoustic signal after the phase modulators over (a) 100 s and (b) 1 h. Output phase is calculated from the I and Q signals, as shown in Fig. 4(a). Sampling rate of the phase is 1000 samples/s in (a). For each data point in (b), the capture time is 1 s with a sampling rate of 1000 samples/s, and the phase is captured at 3-s intervals, allowing data transfer from the oscilloscope.

LNSa. As the thermal conductivity of LN is lower than that of sapphire, the bulk LN modulators feature a larger phase shift per unit heater power than LNSa modulators, while LNSa modulators show a larger frequency bandwidth. For the integration of other LN devices on a single chip, such as optical waveguides and modulators, rib waveguides fabricated using thin-film LN on sapphire can simultaneously guide acoustic waves and optical light, while the bulk LN platform may require an overlaid high-refractive-index material, such as silicon, or an ion-diffused region to guide the optical light. Compared to electroacoustic modulators [45], our thermoacoustic modulators show a larger tuning range and require much smaller electrical voltages despite static power consumption. To further improve the modulation response, one can develop thermoacoustic modulators using suspended LN thin films. Tunable acoustic wave filters can be developed by integrating microheaters with acoustic cavities or phononic crystals. Utilizing the temperature gradient generated by the microheater on a chip, one can develop efficient and compact phase arrays using acoustic waveguides, which have wide applications in beam formation. We believe that our thermal control of acoustic waves could enable the future development of acoustic wave circuits for microwave signal processing.

ACKNOWLEDGMENT

This work is supported by DOE HEADS-QON Grant No. DE-SC0020376, ONR Grant No. N00014-20-1-2425, DOD Grant No. FA8702-15-D-0001, and Raytheon Grant No. A40210. L.S. acknowledges funding from Virginia Tech Foundation. N.S. acknowledges funding from the AQT Intelligent Quantum Networks and Technologies (INQNET) research program.

[1] S. Gong, R. Lu, Y. Yang, L. Gao, and A. E. Hassanien, Microwave acoustic devices: Recent advances and outlook, IEEE J. Microwaves **1**, 601 (2021).

[2] P. Delsing, A. N. Cleland, M. J. A. Schuetz, J. Knörzer, G. Giedke, J. I. Cirac, K. Srinivasan, M. Wu, K. C. Balram, C. Bäuerle *et al.*, The 2019 surface acoustic waves roadmap, J. Phys. D: Appl. Phys. **52**, 353001 (2019).

[3] C. Campbell, *Surface Acoustic Wave Devices and their Signal Processing Applications* (Academic Press, San Diego, CA, 1989).

[4] R. Lu and S. Gong, Rf acoustic microsystems based on suspended lithium niobate thin films: Advances and outlook, J. Micromech. Microeng. **31**, 114001 (2021).

[5] K. Yamanouchi, T. Meguro, Y. Wagatsuma, H. Odagawa, and K. Yamamoto, Nanometer electrode fabrication technology using anodic oxidation resist and application to unidirectional surface acoustic wave transducers, Jpn. J. Appl. Phys. **33**, 3018 (1994).

[6] Y. Takagaki, P. V. Santos, E. Wiebicke, O. Brandt, H. P. Schönherr, and K. H. Ploog, Superhigh-frequency surface-acoustic-wave transducers using AlN layers grown on SiC substrates, Appl. Phys. Lett. **81**, 2538 (2002).

[7] I. V. Kukushkin, J. H. Smet, L. Höppel, U. Waizmann, M. Riek, W. Wegscheider, and K. von Klitzing, Ultrahigh-frequency surface acoustic waves for finite wave-vector spectroscopy of two-dimensional electrons, Appl. Phys. Lett. **85**, 4526 (2004).

[8] Y. Yang, R. Lu, T. Manzaneque, and S. Gong, in *2018 IEEE International Frequency Control Symposium* (IEEE, Olympic Valley, CA, 2018).

[9] Y. Yang, R. Lu, L. Gao, and S. Gong, 10–60-GHz electromechanical resonators using thin-film lithium niobate, IEEE Trans. Microwave Theory Tech. **68**, 5211 (2020).

[10] S. J. Whiteley, G. Wolfowicz, C. P. Anderson, A. Bourassa, H. Ma, M. Ye, G. Koolstra, K. J. Satzinger, M. V. Holt, F. J. Heremans, *et al.*, Spin–phonon interactions in silicon

carbide addressed by Gaussian acoustics, Nat. Phys. **15**, 490 (2019).

[11] S. Maity, L. Shao, S. Bogdanović, S. Meesala, Y.-I. Sohn, N. Sinclair, B. Pingault, M. Chalupnik, C. Chia, L. Zheng, *et al.*, Coherent acoustic control of a single silicon vacancy spin in diamond, Nat. Commun. **11**, 193 (2020).

[12] S. Maity, B. Pingault, G. Joe, M. Chalupnik, D. Assumpção, E. Cornell, L. Shao, and M. Lončar, Mechanical Control of a Single Nuclear Spin, Phys. Rev. X **12**, 011056 (2022).

[13] Y. Chu, P. Kharel, W. H. Renninger, L. D. Burkhart, L. Frunzio, P. T. Rakich, and R. J. Schoelkopf, Quantum acoustics with superconducting qubits, Science **358**, 199 (2017).

[14] R. Manenti, A. F. Kockum, A. Patterson, T. Behrle, J. Rahamim, G. Tancredi, F. Nori, and P. J. Leek, Circuit quantum acoustodynamics with surface acoustic waves, Nat. Commun. **8**, 975 (2017).

[15] K. J. Satzinger, Y. P. Zhong, H. S. Chang, G. A. Peairs, A. Bienfait, M. H. Chou, A. Y. Cleland, C. R. Conner, E. Dumur, J. Grebel, *et al.*, Quantum control of surface acoustic-wave phonons, Nature **563**, 661 (2018).

[16] P. Arrangoiz-Arriola, E. A. Wollack, Z. Wang, M. Pechal, W. Jiang, T. P. McKenna, J. D. Witmer, R. Van Laer, and A. H. Safavi-Naeini, Resolving the energy levels of a nanomechanical oscillator, Nature **571**, 537 (2019).

[17] A. Bienfait, K. J. Satzinger, Y. P. Zhong, H.-S. Chang, M.-H. Chou, C. R. Conner, É. Dumur, J. Grebel, G. A. Peairs, R. G. Povey, and A. N. Cleland, Phonon-mediated quantum state transfer and remote qubit entanglement, Science **364**, 368 (2019).

[18] G. Andersson, B. Suri, L. Guo, T. Aref, and P. Delsing, Non-exponential decay of a giant artificial atom, Nat. Phys. **15**, 1123 (2019).

[19] M. V. Gustafsson, T. Aref, A. F. Kockum, M. K. Ekström, G. Johansson, and P. Delsing, Propagating phonons coupled to an artificial atom, Science **346**, 207 (2014).

[20] M. Mirhosseini, A. Sipahigil, M. Kalaee, and O. Painter, Superconducting qubit to optical photon transduction, Nature **588**, 599 (2020).

[21] W. Jiang, C. J. Sarabalis, Y. D. Dahmani, R. N. Patel, F. M. Mayor, T. P. McKenna, R. Van Laer, and A. H. Safavi-Naeini, Efficient bidirectional piezo-optomechanical transduction between microwave and optical frequency, Nat. Commun. **11**, 1166 (2020).

[22] L. Shao, M. Yu, S. Maity, N. Sinclair, L. Zheng, C. Chia, A. Shams-Ansari, C. Wang, M. Zhang, K. Lai, and M. Lončar, Microwave-to-optical conversion using lithium niobate thin-film acoustic resonators, Optica **6**, 1498 (2019).

[23] B. J. Eggleton, C. G. Poulton, P. T. Rakich, M. J. Steel, and G. Bahl, Brillouin integrated photonics, Nat. Photonics **13**, 664 (2019).

[24] M. Forsch, R. Stockill, A. Wallucks, I. Marinković, C. Gärtner, R. A. Norte, F. van Otten, A. Fiore, K. Srinivasan, and S. Gröblacher, Microwave-to-optics conversion using a mechanical oscillator in its quantum ground state, Nat. Phys. **16**, 69 (2020).

[25] G. S. MacCabe, H. Ren, J. Luo, J. D. Cohen, H. Zhou, A. Sipahigil, M. Mirhosseini, and O. Painter, Nano-acoustic resonator with ultralong phonon lifetime, Science **370**, 840 (2020).

[26] Q. Liu, H. Li, and M. Li, Electromechanical Brillouin scattering in integrated optomechanical waveguides, Optica **6**, 778 (2019).

[27] S. A. Tadesse and M. Li, Sub-optical wavelength acoustic wave modulation of integrated photonic resonators at microwave frequencies, Nat. Commun. **5**, 5402 (2014).

[28] M. B. Assouar, O. Elmazria, P. Kirsch, P. Alnot, V. Mortet, and C. Tiusan, High-frequency surface acoustic wave devices based on AlN/diamond layered structure realized using *e*-beam lithography, J. Appl. Phys. **101**, 114507 (2007).

[29] L. Fan, X. Sun, C. Xiong, C. Schuck, and H. X. Tang, Aluminum nitride piezo-acousto-photonic crystal nanocavity with high quality factors, Appl. Phys. Lett. **102**, 153507 (2013).

[30] Z. Schaffer and G. Piazza, in *2020 IEEE International Ultrasonics Symposium (IUS)* (2020), pp. 1.

[31] Z. A. Schaffer, G. Piazza, S. Mishin, and Y. Oshmyansky, in *2020 IEEE 33rd International Conference on Micro Electro Mechanical Systems (MEMS)* (2020), pp. 1281.

[32] J. Wang, M. Park, S. Mertin, T. Pensala, F. Ayazi, and A. Ansari, A film bulk acoustic resonator based on ferroelectric aluminum scandium nitride films, J. Microelectromech. Syst. **29**, 741 (2020).

[33] X.-B. Xu, J.-Q. Wang, Y.-H. Yang, W. Wang, Y.-L. Zhang, B.-Z. Wang, C.-H. Dong, L. Sun, G.-C. Guo, and C.-L. Zou, High-frequency traveling-wave phononic cavity with submicron wavelength, Appl. Phys. Lett. **120**, 163503 (2022).

[34] E. B. Magnusson, B. H. Williams, R. Manenti, M. S. Nam, A. Nersisyan, M. J. Peterer, A. Ardavan, and P. J. Leek, Surface acoustic wave devices on bulk ZnO crystals at low temperature, Appl. Phys. Lett. **106**, 063509 (2015).

[35] T. Kimura, M. Kadota, and Y. Ida, in *2010 IEEE MTT-S International Microwave Symposium* (2010), pp. 1740.

[36] T. Takai, H. Iwamoto, Y. Takamine, H. Yamazaki, T. Fuyutsume, H. Kyoya, T. Nakao, H. Kando, M. Hiramoto, T. Toi, *et al.*, High-performance SAW resonator on new multilayered substrate using $LiTaO_3$ crystal, IEEE Trans. Ultrason. Ferroelectr. Freq. Control **64**, 1382 (2017).

[37] M.-H. Li, R. Lu, T. Manzaneque, and S. Gong, Low phase noise rf oscillators based on thin-film lithium niobate acoustic delay lines, J. Microelectromech. Syst. **29**, 129 (2020).

[38] L. Shao, S. Maity, L. Zheng, L. Wu, A. Shams-Ansari, Y.-I. Sohn, E. Puma, M. N. Gadalla, M. Zhang, C. Wang, *et al.*, Phononic Band Structure Engineering for High-Q Gigahertz Surface Acoustic Wave Resonators on Lithium Niobate, Phys. Rev. Appl. **12**, 014022 (2019).

[39] C. J. Sarabalis, R. Van Laer, R. N. Patel, Y. D. Dahmani, W. Jiang, F. M. Mayor, and A. H. Safavi-Naeini, Acousto-optic modulation of a wavelength-scale waveguide, Optica **8**, 477 (2021).

[40] F. M. Mayor, W. Jiang, C. J. Sarabalis, T. P. McKenna, J. D. Witmer, and A. H. Safavi-Naeini, Gigahertz Phononic Integrated Circuits on Thin-Film Lithium Niobate on Sapphire, Phys. Rev. Appl. **15**, 014039 (2021).

[41] M. Bousquet, P. Perreau, C. Maeder-Pachurka, A. Joulie, F. Delaguillaumie, J. Delprato, G. Enyedi, G. Castellan, C.

Elleouet, T. Farjot, C. Billard, and A. Reinhardt, in *2020 IEEE International Ultrasonics Symposium (IUS)* (2020), pp. 1.

[42] T. C. Lee, J. T. Lee, M. A. Robert, S. Wang, and T. A. Rabson, Surface acoustic wave applications of lithium niobate thin films, Appl. Phys. Lett. **82**, 191 (2003).

[43] R. Fleury, D. L. Sounas, C. F. Sieck, M. R. Haberman, and A. Alù, Sound isolation and giant linear nonreciprocity in a compact acoustic circulator, Science **343**, 516 (2014).

[44] Y. Yu, G. Michetti, M. Pirro, A. Kord, D. L. Sounas, Z. Xiao, C. Cassella, A. Alu, and M. Rinaldi, Radio frequency magnet-free circulators based on spatiotemporal modulation of surface acoustic wave filters, IEEE Trans. Microwave Theory Tech. **67**, 4773 (2019).

[45] L. Shao, D. Zhu, M. Colangelo, D. H. Lee, N. Sinclair, Y. Hu, P. T. Rakich, K. Lai, K. K. Berggren, and M. Loncar, Electrical control of surface acoustic waves, Nat. Electron. **5**, 348 (2022).

[46] H. Mansoorzare and R. Abdolvand, Acoustoelectric nonreciprocity in lithium niobate-on-silicon delay lines, IEEE Electron Device Lett. **41**, 1444 (2020).

[47] L. Bandhu and G. R. Nash, Controlling the properties of surface acoustic waves using graphene, Nano Res. **9**, 685 (2016).

[48] R. Sasaki, Y. Nii, Y. Iguchi, and Y. Onose, Nonreciprocal propagation of surface acoustic wave in Ni/$LiNbO_3$, Phys. Rev. B **95**, 020407 (2017).

[49] J. Zhang, B. Peng, ŞK Özdemir, Y.-X. Liu, H. Jing, X.-Y. Lü, Y.-L. Liu, L. Yang, and F. Nori, Giant nonlinearity via breaking parity-time symmetry: A route to low-threshold phonon diodes, Phys. Rev. B **92**, 115407 (2015).

[50] L. Shao, W. Mao, S. Maity, N. Sinclair, Y. Hu, L. Yang, and M. Lončar, Non-reciprocal transmission of microwave acoustic waves in nonlinear parity–time symmetric resonators, Nat. Electron. **3**, 267 (2020).

[51] R. Fleury, D. Sounas, and A. Alu, An invisible acoustic sensor based on parity-time symmetry, Nat. Commun. **6**, 5905 (2015).

[52] D. Hatanaka, I. Mahboob, K. Onomitsu, and H. Yamaguchi, Phonon waveguides for electromechanical circuits, Nat. Nanotechnol. **9**, 520 (2014).

[53] J. C. Taylor, E. Chatterjee, W. F. Kindel, D. Soh, and M. Eichenfield, Reconfigurable quantum phononic circuits via piezo-acoustomechanical interactions, npj Quantum Inf. **8**, 19 (2022).

[54] R. B. Ward, Temperature coefficients of SAW delay and velocity for *Y*-cut and rotated $LiNbO_3$, IEEE Trans. Ultrason. Ferroelectr. Freq. Control **37**, 481 (1990).